View metadata, citation and similar papers at core.ac.uk
brought to you by CORE
provided by University of Liverpool Repository

Design and Implementation of Perturbation Observer based Robust Passivity-based Control for VSC-MTDC Systems Considering Offshore Wind Power Integration

Yiyan Sang Bo Yang Wei Yao Lin Jiang

November 14, 2018

Abstract

With the increasing penetration of renewable energy sources especially wind power, voltage source converter based multi-terminal high voltage direct current (VSC-MTDC) systems are starting to be commissioned. However, concentrated integration of large scale wind power demands stronger robustness against power fluctuation and system disturbances to increase the reliability of the whole system. This paper proposes a perturbation observer based robust passivity-based control (PORPC) for VSC-MTDC systems connected to an offshore wind farm to meet the demands. The aggregated effect of system nonlinearities, parameter uncertainties, unmodelled dynamics and external disturbances includes grid faults and time-varying wind power output is estimated by a linear perturbation observer (PO) and fully compensated by a passive controller, thus no accurate VSC-MTDC system model is required. The proposed scheme attempts to regulate DC voltage and reactive power at the rectifier side, as well as active power and reactive power at the inverters side connected to an offshore wind farm. Besides, a DC link voltage droop controller is introduced so as to provide immediate response to the grid unbalance situation Moreover, a noticeable robustness against parameter uncertainties can be achieved as no accurate system model is needed. Case studies are carried out to compare the performance of PORPC to other typical approaches. Lastly, a hardware-in-the-loop (HIL) test is undertaken via dSPACE simulators which validates its implementation feasibility.

1 Introduction

Large-scale integration of offshore wind power to the main grid presents a number of technical, economical, and environmental challenges [1]. With the capacity and distance of offshore wind farm increases, conventional AC transmission system displays serious drawbacks, e.g., long AC cables usually produce significant amount of capacitive current which often limits the transmission capacity and requires extra reactive power compensation. Besides, AC connections require to be operated synchronously between the wind farm and the power grid. Therefore, all faults occur in either grid are propagated in the other [2].

Currently, line-commutated converter (LCC) based HVDC (LCC-HVDC) is regarded as a mature technology on overhead lines and an economical solution with higher power ratings. However, for connecting offshore wind farms, its disadvantages are obvious: coarser reactive power control and cannot control the active power and reactive power independently, requiring strong AC power source to maintain operation and own black-start capability, requiring AC&DC harmonic filter to eliminate generated harmonic distortion. Moreover, extra auxiliary equipments like filter and power source comparing with VSC cannot meet the space requirements of offshore substation application. Therefore, there is no LCC-HVDC offshore substation in operation. In contrast, voltage source converter based high voltage direct current (VSC-HVDC) technology using pulse-width modulation (PWM) with lower harmonic distortion of AC-side voltage, as well as fewer auxiliary filters, attracts noticeable attention around the globe. It is more suitable for offshore wind farm connection, in which active and reactive power can be independently controlled and VSCs are able to operate in weak or even passive networks [3]. In the Nanao project [4] which is the world's first multi-terminal VSC-HVDC transmission project in operation. The project is designed with ratings of $\pm$ 160kV/200MW-100MW-50MW to transmit dispersed, intermittent wind power generated on Nanao island into the mainland. A crucial task of VSC-HVDC system is how to design proper control schemes to achieve satisfactory system performance.

In general, linear control methods using proportional-integral (PI) loops are widely adopted for VSC-HVDC systems. However, the VSC-HVDC systems with wind farm connection are highly nonlinear resulted from converters, wind turbine aerodynamics, highly stochastic wind speed, and power grids with various system uncertainties like power angle and uncertain output impedance. Hence, their control performance may be dramatically degraded as its control parameters are determined from one-point linearization model [5]. In order to tackle this thorny problem, robust controller for VSC-HVDC systems is required to ensure a consistent control performance under various system uncertainties, such as adaptive backstepping [6] and robust sliding-mode control [7], which have been developed to greatly improve system robustness via estimation compensation of unknown constant or slow-varying system parameters. However, the parameter estimates via these estimation functions may drift in the presence of measurement noise and greatly increase the energy consumption.

Furthermore, the above applications are merely applied to two-terminal VSC-HVDC systems. In the multi-terminal VSC-HVDC (VSC-MTDC) system framework, not only the DC voltage and power transmission stability need to be self-controlled, but also an appropriate coordination among different terminals are needed. Thus far, several coordinated control schemes have been developed for VSC-MTDC systems, such as adaptive droop control [8], which can share the burden according to the available headroom of each converter station. Meanwhile, an adaptive backstepping droop controller is proposed in [9], which can adaptively tune the droop gains to enhance control performance of traditional droop controllers by considering DC cable dynamics. Moreover, power-dependent droop-based control strategy is proposed in [10] so as to offer enhanced dynamic responses during AC/DC faults and large power scheduling changes.

Generally speaking, the aforementioned approaches merely consider the control problems as a pure mathematical issue, while the physical/engineering background of the given object is somehow ignored. The passivity-based control (PC) offers a powerful tool to beneficially exploit the physical property of a given engineering problem, upon energy interconnection and assignment, to achieve a satisfactory transient responses with relatively low control efforts [11]. However, conventional PC [12] is highly sensitive to the uncertain system parameters and requires a detailed system model. To handle such issue, this paper proposes a perturbation observer based robust passivity-based control (PORPC) scheme for an N-terminal VSC-MTDC system, in which the combinatorial effect of interaction between different terminals, unmodelled dynamics and unknown time-varying external disturbances is aggregated into a perturbation, which is estimated online by a high-gain state and perturbation observer (HGSPO) [13, 14] and can be represented as a chained-integrator system associated with matched nonlinearities and disturbances. Moreover, PORPC does not require an accurate VSC-MTDC model and only the DC voltage, active and reactive power need to be measured. Furthermore, it provides a faster transient response with low control efforts as passification [12] is adopted to carefully reshape the system damping.

The main novelties and contributions of this paper can be summarized as follows:

- The active/reactive power control can achieve reliable and robust decoupling control with fast responses in randomly time-varying wind power outputs and severe grid faults;

- Compared to reference [14], there are three improvements listed as follows, (1) a DC link voltage droop controller with appropriate droop constant is introduced into PORPC of each terminal, which can provide immediate response to the grid unbalanced conditions, (2) The wind farm modelling is considered during the controller design process, in which the controller parameters are modified during this case, (3) The implementation feasibility of PORPC is validated through several case studies on Simulink and real-time hardware in-loop (HIL) test based on dSPACE platform;

- The DC voltage regulation control aims to rapidly compensate various DC cable modelling uncertainties, such as unpredictable power losses, inaccurate series resistance and inductance, and external disturbances resulted from randomly time-varying wind speed conditions;

The rest of the paper is organized as follows. In Section II, the modelling of the VSC-MTDC system is presented. In Section III, the PORPC-based rec-

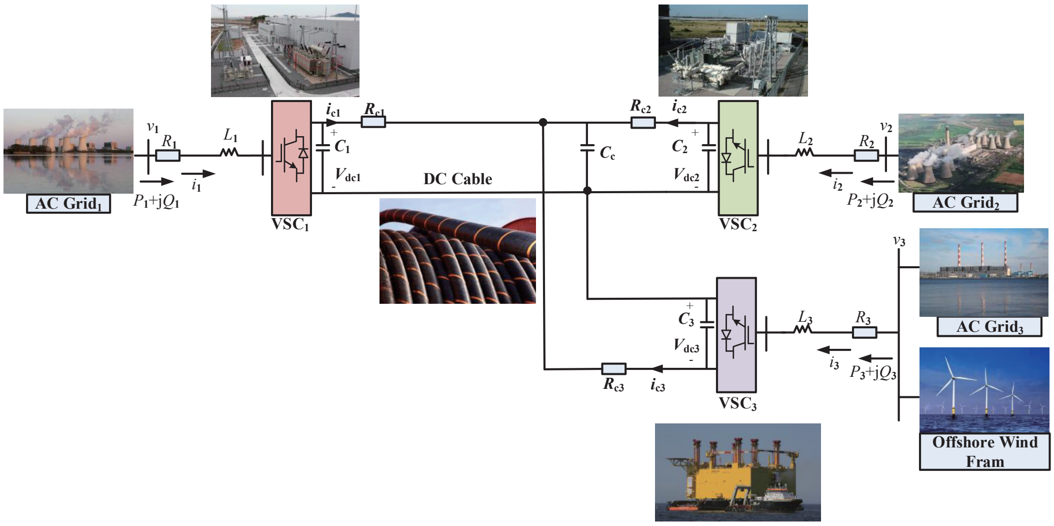

Figure 1: The configuration of a three-terminal radial VSC-MTDC system connecting to an offshore wind farm.

tifier controller and inverter controller are developed. Simulation and HIL test results are provided in Section IV and V, respectively. Finally, conclusions are summarized in Section VI.

2 VSC-MTDC System with Offshore Wind Farm Modelling

The configuration of a three-terminal radial VSC-MTDC system connected to an offshore wind farm is illustrated by Fig. 1, in which the rectifier regulates the DC voltage and reactive power of AC grid$_1$, while one inverter regulates the active and reactive power of the AC grid$_2$ and another inverter regulates the active and reactive power of the offshore wind farm with AC grid$_3$. Only the balanced condition is considered, e.g., the three phases have identical parameters and their voltages and currents have the same amplitude while each phase shifts 120° between themselves. On the ith AC terminal of the three-terminal VSC-MTDC system, the system dynamics of VSC can be expressed at the angular frequency ω_i as [8]

$$\begin{cases} \dot{I}_{\mathrm{d}i} = -\frac{R_i}{L_i} I_{\mathrm{d}i} + \omega_i I_{\mathrm{q}i} + \frac{V_{\mathrm{sq}i}}{L_i} + \frac{u_{\mathrm{d}i}}{L_i} \\ \dot{I}_{\mathrm{q}i} = -\frac{R_i}{L_i} I_{\mathrm{q}i} + \omega_i I_{\mathrm{d}i} + \frac{V_{\mathrm{sd}i}}{L_i} + \frac{u_{\mathrm{q}i}}{L_i} \end{cases} \tag{1}$$

where $I_{\mathrm{d}i}$ and $I_{\mathrm{q}i}$ are the ith d-axis and q-axis AC currents; $V_{\mathrm{sd}i}$ and $V_{\mathrm{sq}i}$ are the ith d-axis and q-axis AC voltages, in the synchronous frame $V_{\mathrm{sd}i} = 0$ and $V_{\mathrm{sq}i} = V_{\mathrm{s}}$; $u_{\mathrm{d}i}$ and $u_{\mathrm{q}i}$ are the ith d-axis and q-axis control inputs; and R_i

and L_i are the aggregated resistance and inductance of the ith AC terminal, respectively.

By neglecting the resistance of VSC reactors and switch losses, the instantaneous active power P_i and reactive power Q_i on the ith AC terminal can be calculated as follows

$$\begin{cases} P_i = \frac{3}{2}(V_{\mathrm{sq}i}I_{\mathrm{q}i} + V_{\mathrm{sd}i}I_{\mathrm{d}i}) = \frac{3}{2}V_{\mathrm{sq}i}I_{\mathrm{q}i} \\ Q_i = \frac{3}{2}(V_{\mathrm{sq}i}I_{\mathrm{d}i} - V_{\mathrm{sd}i}I_{\mathrm{q}i}) = \frac{3}{2}V_{\mathrm{sq}i}I_{\mathrm{d}i} \end{cases} \tag{2}$$

The DC link dynamics can be expressed by

$$\begin{cases} \dot{V}_{\mathrm{dc}i} = \frac{1}{V_{\mathrm{dc}i}C_i}P_i - \frac{1}{C_i}I_{\mathrm{c}i} \\ \dot{I}_{\mathrm{c}i} = \frac{1}{L_{\mathrm{c}i}}V_{\mathrm{dc}i} - \frac{R_{\mathrm{c}i}}{L_{\mathrm{c}i}}I_{\mathrm{c}i} - \frac{1}{L_{\mathrm{c}i}}V_{\mathrm{cc}} \end{cases} \tag{3}$$

The topology of a three-terminal VSC-MTDC system is illustrated by Fig.1, in which the dynamics of the common DC capacitor can be obtained according to the Kirchhoff's current law as

$$\dot{V}_{\mathrm{cc}} = \frac{1}{C_{\mathrm{c}}}\sum_{i=1}^{3} I_{\mathrm{c}i} \tag{4}$$

where C_i and C_{c} are the ith DC link capacitance and the common DC capacitance which voltages are denoted by $V_{\mathrm{dc}i}$ and V_{cc}; $R_{\mathrm{c}i}$ and $L_{\mathrm{c}i}$ are the resistance and inductance of the ith DC cable; and $I_{\mathrm{c}i}$ is the current through the ith DC cable. The featured DC cable model corresponds to a simplified equivalence of a cable connection, because an overhead line could be represented by an inductive element [3]. This is a reasonable approximation for the purpose of control systems analysis. To this end, the global model of the three-terminal VSC-MTDC system can be written as follows

$$\begin{cases} \dot{I}_{\mathrm{d}i} = -\frac{R_i}{L_i}I_{\mathrm{d}i} + \omega_i I_{\mathrm{q}i} + \frac{V_{\mathrm{sq}i}}{L_i} + \frac{u_{\mathrm{d}i}}{L_i} \\ \dot{I}_{\mathrm{q}i} = -\frac{R_i}{L_i}I_{\mathrm{q}i} + \omega_i I_{\mathrm{d}i} + \frac{u_{\mathrm{q}i}}{L_i} \\ \dot{V}_{\mathrm{dc}i} = \frac{3V_{\mathrm{sq}i}I_{\mathrm{q}i}}{2V_{\mathrm{dc}i}C_i} - \frac{1}{C_i}I_{\mathrm{c}i} \\ \dot{I}_{\mathrm{c}i} = \frac{1}{L_{\mathrm{c}i}}V_{\mathrm{dc}i} - \frac{R_{\mathrm{c}i}}{L_{\mathrm{c}i}}I_{\mathrm{c}i} - \frac{1}{L_{\mathrm{c}i}}V_{\mathrm{cc}} \\ \dot{V}_{\mathrm{cc}} = \frac{1}{C_{\mathrm{c}}}\sum_{i=1}^{N} I_{\mathrm{c}i} \end{cases} , i = 1, \ldots, 3 \tag{5}$$

Besides normal grid models which are usually considered as fixed power sources that connect to the VSC-MTDC model, the grid with high wind power penetration (20%) is considered as well. The offshore wind farm simulated in this paper adopts an aggregated model such that a lumped wind turbine is used to represent the whole wind farm [15]. In particular, the wind turbine dynamics is represented by a two-mass model while the blade pitch angle is assumed to be a constant. According to wind turbine aerodynamics, the mechanical power P_{m} extracted from wind is described as follows [16, 17]

$$P_{\mathrm{m}} = \frac{1}{2}\rho A_{\mathrm{r}} c_{\mathrm{p}}(\lambda, \theta) v_{\omega}^3 \tag{6}$$

where P_{m} is the power extracted from the wind; ρ is air density; A_{r} is the area covered by the rotor; v_{ω} is the wind speed; and c_{p} is the power coefficient; θ is the pitch angle of rotor blades; λ is the tip speed ratio which $\lambda = \frac{v_{\mathrm{t}}}{v_{\omega}}$ with v_{t} is blade tip speed [18, 19]. Here c_{p} can be described by

$$c_{\mathrm{p}}(\lambda, \theta) = 0.73(\frac{151}{\lambda_i} - 0.58\theta - 0.002\theta^{2.14} - 13.2)e^{-18.4/\lambda_i} \tag{7}$$

where

$$\lambda_i = \frac{1}{\frac{1}{\lambda - 0.02\theta} - \frac{0.003}{\theta^3 + 1}} \tag{8}$$

3 PORPC Design for the VSC-MTDC System

3.1 Rectifier controller design

Denote the first VSC as the rectifier such that DC voltage V_{dc1} and reactive power Q_1 can be regulated to their references V_{dc1}^* and Q_1^*, respectively. Define the tracking error

$\mathbf{e}_1 = [e_{11}, e_{12}]^{\mathrm{T}} = [V_{\mathrm{dc1}} - V_{\mathrm{dc1}}^*, Q_1 - Q_1^*]^{\mathrm{T}}$,

Differentiate $\mathbf{e}_1$ until control inputs u_{q1} and u_{d1} appear explicitly, gives

$$\left\{ \begin{array}{ll} \ddot{e}_{11} & = \frac{3V_{\mathrm{sq1}}}{2C_1 V_{\mathrm{dc1}}} \Big[-\frac{R_1}{L_1} I_{\mathrm{q1}} + \omega_1 I_{\mathrm{d1}} \\ & -\frac{I_{\mathrm{q1}}}{C_j V_{\mathrm{dc1}}} \Big(\frac{3V_{\mathrm{sq1}} I_{\mathrm{q1}}}{2V_{\mathrm{dc1}}} - I_{\mathrm{c1}} \Big) \Big] + \frac{3V_{\mathrm{sq1}}}{2C_1 L_1 V_{\mathrm{dc1}}} u_{\mathrm{q1}} \\ & -\frac{1}{C_1 L_{\mathrm{c1}}} (V_{\mathrm{dc1}} - R_{\mathrm{c1}} I_{\mathrm{c1}} - V_{\mathrm{cc}}) - \ddot{V}_{\mathrm{dc1}}^* \\ \dot{e}_{12} & = \frac{3V_{\mathrm{sq1}}}{2} \Big(-\frac{R_1}{L_1} I_{\mathrm{d1}} + \omega_1 I_{\mathrm{q1}} + \frac{V_{\mathrm{sq1}}}{L_1} \Big) + \frac{3V_{\mathrm{sq1}}}{2L_1} u_{\mathrm{d1}} - \dot{Q}_1^* \end{array} \right. \tag{9}$$

It can be seen that system (9) includes two decoupled SISO subsystems, in which V_{dc1} is controlled by u_{q1} and Q_1 is controlled by u_{d1}, respectively.

The perturbations of system (9) are defined as

$$\begin{aligned} \Psi_{11}(\cdot) = & \frac{3V_{\mathrm{sq1}}}{2C_1 V_{\mathrm{dc1}}} \Big[-\frac{R_1}{L_1} I_{\mathrm{q1}} + \omega_1 I_{\mathrm{d1}} \\ & - \frac{I_{\mathrm{q1}}}{C_1 V_{\mathrm{dc1}}} \Big(\frac{3V_{\mathrm{sq1}} I_{\mathrm{q1}}}{2V_{\mathrm{dc1}}} I_{\mathrm{c1}} \Big) \Big] \\ & - \frac{1}{C_1 L_{\mathrm{c1}}} (V_{\mathrm{dc1}} - R_{\mathrm{c1}} I_{\mathrm{c1}} - V_{\mathrm{cc}}) \\ & + (\frac{3V_{\mathrm{sq1}}}{2C_1 L_1 V_{\mathrm{dc1}}} - b_{11}) u_{\mathrm{q1}} \end{aligned} \tag{10}$$

$$\begin{aligned} \Psi_{12}(\cdot) = & \frac{3V_{\mathrm{sq1}}}{2} \left(-\frac{R_1}{L_1} I_{\mathrm{d1}} + \omega_1 I_{\mathrm{q1}} + \frac{V_{\mathrm{sq1}}}{L_1} \right) \\ & + (\frac{3V_{\mathrm{sq1}}}{2L_1} - b_{12}) u_{\mathrm{d1}} \end{aligned} \tag{11}$$

And system (9) can be expressed by

$$\left\{\begin{array}{l} \ddot{e}_{11} = \Psi_{11}(\cdot) + b_{11}u_{\mathrm{q1}} - \ddot{V}^*_{\mathrm{dc1}} \\ \dot{e}_{12} = \Psi_{12}(\cdot) + b_{12}u_{\mathrm{d1}} - \dot{Q}^*_1 \end{array}\right. \tag{12}$$

where b_{11} and b_{12} are constant control gains.

A third-order HGSPO is designed to estimate $\Psi_{11}(\cdot)$ as

$$\left\{\begin{array}{l} \dot{\hat{V}}_{\mathrm{dc1}} = \frac{\alpha_{11}}{\epsilon}(V_{\mathrm{dc1}} - \hat{V}_{\mathrm{dc1}}) + \hat{\dot{V}}_{\mathrm{dc1}} \\ \dot{\hat{\dot{V}}}_{\mathrm{dc1}} = \hat{\Psi}_{11}(\cdot) + \frac{\alpha_{12}}{\epsilon^2}(V_{\mathrm{dc1}} - \hat{V}_{\mathrm{dc1}}) + b_{11}u_{\mathrm{q1}} \\ \dot{\hat{\Psi}}_{11}(\cdot) = \frac{\alpha_{13}}{\epsilon^3}(V_{\mathrm{dc1}} - \hat{V}_{\mathrm{dc1}}) \end{array}\right. \tag{13}$$

Then a second-order high-gain perturbation observer (HGPO) is designed to estimate $\Psi_{12}(\cdot)$ as

$$\left\{\begin{array}{l} \dot{\hat{Q}}_1 = \hat{\Psi}_{12}(\cdot) + \frac{\alpha'_{11}}{\epsilon}(Q_1 - \hat{Q}_1) + b_{12}u_{\mathrm{d1}} \\ \dot{\hat{\Psi}}_{12}(\cdot) = \frac{\alpha'_{12}}{\epsilon^2}(Q_1 - \hat{Q}_1) \end{array}\right. \tag{14}$$

where α_{11}, α_{12}, α_{13}, α'_{11}, and α'_{12} are observer gains, with $0 < \epsilon \ll 1$.

The PORPC for system (9) using the estimate of states and perturbations is designed as

$$\left\{\begin{array}{ll} u_{\mathrm{q1}} & = b_{11}^{-1}[-\hat{\Psi}_{11}(\cdot) - k_{11}(\hat{V}_{\mathrm{dc1}} - V^*_{\mathrm{dc1}}) \\ & \quad -k_{12}(\hat{\dot{V}}_{\mathrm{dc1}} - \dot{V}^*_{\mathrm{dc1}}) + \ddot{V}^*_{\mathrm{dc1}} + \nu_{11}] \\ u_{\mathrm{d1}} & = b_{12}^{-1}(-\hat{\Psi}_{12}(\cdot) - k'_{11}(\hat{Q}_1 - Q^*_1) + \dot{Q}^*_1 + \nu_{12}) \end{array}\right. \tag{15}$$

where k_{11}, k_{12} and k'_{11} are feedback control gains and $\mathbf{V}_1 = [\nu_{11}, \nu_{12}]^{\mathrm{T}}$ is an additional system input.

Choose the output of system (9) as $\mathbf{Y}_1 = [Y_{11}, Y_{12}]^{\mathrm{T}} = [\dot{V}_{\mathrm{dc1}} - \dot{V}^*_{\mathrm{dc1}}, Q_1 - Q^*_1]^{\mathrm{T}}$. Then let $\mathbf{V}_1 = [-\lambda_{11}Y_{11}, -\lambda_{12}Y_{12}]^{\mathrm{T}}$, where λ_{11} and λ_{12} are some positive constants to inject an extra system damping into system (9). Based on the passivity theory, the closed-loop system is output strictly passive from output $\mathbf{Y}_1$ to input $\mathbf{V}_1$ [11].

Constant gains b_{11} and b_{12} must satisfy the following inequalities to guarantee the convergence of estimation error when the VSC operates within its normal region:

$$\begin{aligned} 3V_{\mathrm{sq1}}/[2C_1L_1V_{\mathrm{dc1}}(1-\theta_{11})] \geq b_{11} \\ \geq 3V_{\mathrm{sq1}}/[2C_1L_1V_{\mathrm{dc1}}(1+\theta_{11})] \end{aligned} \tag{16}$$

$$3V_{\mathrm{sq1}}/[2L_1(1-\theta_{12})] \geq b_{12} \geq 3V_{\mathrm{sq1}}/[2L_1(1+\theta_{12})] \tag{17}$$

where $0 < \theta_{11} < 1$ and $0 < \theta_{12} < 1$.

During the most severe disturbance, both DC voltage and reactive power reduce from their initial values to around zero within a short period of time Δ. Thus the boundary values of the estimate of states and perturbations are limited as $|\hat{V}_{\mathrm{dc1}}| \leq |V^*_{\mathrm{dc1}}|$, $|\hat{\dot{V}}_{\mathrm{dc1}}| \leq |V^*_{\mathrm{dc1}}|/\Delta$, $|\hat{\Psi}_{11}(\cdot)| \leq |V^*_{\mathrm{dc1}}|/\Delta^2$, $|\hat{Q}_1| \leq |Q^*_1|$, and $|\hat{\Psi}_{12}(\cdot)| \leq |Q^*_1|/\Delta$, respectively.

3.2 Inverter controller design

The second and third VSCs are chosen as the inverters which regulate active power P_k and reactive power Q_k to their references P_k^* and Q_k^*, respectively, where $k = 2, 3$. Define tracking error with droop controller embedded [20]

$$\mathbf{e}_k = [e_{k1}, e_{k2}]^{\mathrm{T}} = [P_k - P_k^* = R(V_{\mathrm{dc}k} - V_{\mathrm{dc}k}^*), Q_k - Q_k^*]^{\mathrm{T}},$$

where $R = \frac{P_{\mathrm{ACrated}k}}{V_{\mathrm{DCrated}k}\rho_k}$ with ρ_k denotes the droop constant,$P_{\mathrm{ACrated}k}$ is the rated power and $V_{\mathrm{DCrated}k}$ is the rated DC voltage of the kth DC terminal.

Remarks 1. The values of the droop constant are designed according to the ratings of the converters. For a fixed droop scheme it is usual to choose $\rho_i P_{\mathrm{ACrated}i} = \rho_j P_{\mathrm{ACrated}j}, \forall i, j$. [8]. In this paper, as 20% wind power is penetrated into terminal 3, the rating of terminal 3 is considered as 120% of terminal 2. Therefore, the droop constant of terminal 2 is chosen to be 85% of the terminal 3 considering power fluctuation of wind generation. After determining the stability region of MTDC system through modal analysis [8], the value droop constant of terminal 2 and terminal 3 are selected to be 0.035 and 0.0295, respectively. Since the droop constant is unequal , the ones with higher values would have dominant contribution from active power control loop. Smaller would ensure lesser deviation in DC link voltages.

Differentiate $\mathbf{e}_k$ until control inputs $u_{\mathrm{q}k}$ and $u_{\mathrm{d}k}$ appear explicitly, it yields

$$\begin{cases} \dot{e}_{k1} = \frac{3V_{\mathrm{sq}k}}{2}\left(-\frac{R_k}{L_k}I_{\mathrm{q}k} - \omega_k I_{\mathrm{d}k}\right) + \frac{3V_{\mathrm{sq}k}}{2L_k}u_{\mathrm{q}k} - \dot{P}_k^* \\ \dot{e}_{k2} = \frac{3V_{\mathrm{sq}k}}{2}\left(-\frac{R_k}{L_k}I_{\mathrm{d}k} + \omega_k I_{\mathrm{q}k} + \frac{V_{\mathrm{sq}k}}{L_k}\right) + \frac{3V_{\mathrm{sq}k}}{2L_k}u_{\mathrm{d}k} - \dot{Q}_k^* \end{cases} \tag{18}$$

It can be seen that system (18) includes two decoupled SISO subsystems, in which P_k is controlled by $u_{\mathrm{q}k}$ and Q_k is controlled by $u_{\mathrm{d}k}$, respectively.

The perturbations of system (18) are defined as

$$\Psi_{k1}(\cdot) = \frac{3V_{\mathrm{sq}k}}{2}\left(-\frac{R_k}{L_k}I_{\mathrm{q}k} - \omega_k I_{\mathrm{d}k}\right) + (\frac{3V_{\mathrm{sq}k}}{2L_k} - b_{k1})u_{\mathrm{q}k} \tag{19}$$

$$\Psi_{k2}(\cdot) = \frac{3V_{\mathrm{sq}k}}{2}\left(-\frac{R_k}{L_k}I_{\mathrm{d}k} + \omega_k I_{\mathrm{q}k} + \frac{V_{\mathrm{sq}k}}{L_k}\right) + (\frac{3V_{\mathrm{sq}k}}{2L_k} - b_{k2})u_{\mathrm{d}k} \tag{20}$$

And system (18) can be expressed by

$$\begin{cases} \dot{e}_{k1} = \Psi_{k1}(\cdot) + b_{k1}u_{\mathrm{q}k} - \dot{P}_k^* \\ \dot{e}_{k2} = \Psi_{k2}(\cdot) + b_{k2}u_{\mathrm{d}k} - \dot{Q}_k^* \end{cases} \tag{21}$$

where b_{k1} and b_{k2} are constant control gains.

A second-order HGPO is designed to estimate $\Psi_{k1}(\cdot)$ as

$$\left\{\begin{array}{l}\dot{\hat{P}}_k = \hat{\Psi}_{k1}(\cdot) + \frac{\alpha_{k1}}{\epsilon}(P_k - \hat{P}_k) + b_{k1}u_{\mathrm{q}k} \\ \dot{\hat{\Psi}}_{k1}(\cdot) = \frac{\alpha_{k2}}{\epsilon^2}(P_k - \hat{P}_k)\end{array}\right. \tag{22}$$

Similarly, a second-order HGPO is designed to estimate $\Psi_{k2}(\cdot)$ as

$$\left\{\begin{array}{l}\dot{\hat{Q}}_k = \hat{\Psi}_{k2}(\cdot) + \frac{\alpha'_{k1}}{\epsilon}(Q_k - \hat{Q}_k) + b_{k2}u_{\mathrm{d}k} \\ \dot{\hat{\Psi}}_{k2}(\cdot) = \frac{\alpha'_{k2}}{\epsilon^2}(Q_k - \hat{Q}_k)\end{array}\right. \tag{23}$$

where α_{k1}, α_{k2}, α'_{k1}, and α'_{k2} are observer gains.

The PORPC for system (18) using the estimate of states and perturbations is designed as

$$\left\{\begin{array}{l}u_{\mathrm{q}k} = b_{k1}^{-1}(-\hat{\Psi}_{k1}(\cdot) - k_{k1}(\hat{P}_k - P_k^*) + \dot{P}_k^* + \nu_{k1}) \\ u_{\mathrm{d}k} = b_{k2}^{-1}(-\hat{\Psi}_{k2}(\cdot) - k'_{k1}(\hat{Q}_k - Q_k^*) + \dot{Q}_k^* + \nu_{k2})\end{array}\right. \tag{24}$$

where k_{k1} and k'_{k1} are feedback control gains and $\mathbf{V}_k = [\nu_{k1}, \nu_{k2}]^{\mathrm{T}}$ is an additional system input.

Choose the output of system (18) as $\mathbf{Y}_k = [Y_{k1}, Y_{k2}]^{\mathrm{T}} = [P_k - P_k^*, Q_k - Q_k^*]^{\mathrm{T}}$. Let $\mathbf{V}_k = [-\lambda_{k1}Y_{k1}, -\lambda_{k2}Y_{k2}]^{\mathrm{T}}$, where λ_{k1} and λ_{k2} are some positive constants to inject an extra system damping into system (18). And the closed-loop system is output strictly passive from output $\mathbf{Y}_k$ to input $\mathbf{V}_k$.

Similarly, constant gains b_{k1} and b_{k2} must satisfy:

$$\begin{array}{c}3V_{\mathrm{sq}k}/[2L_k(1-\theta_{k1})] \geq b_{k1} \geq 3V_{\mathrm{sq}k}/[2L_k(1+\theta_{k1})] \\ 3V_{\mathrm{sq}k}/[2L_k(1-\theta_{k2})] \geq b_{k2} \geq 3V_{\mathrm{sq}k}/[2L_k(1+\theta_{k2})]\end{array}$$

where $0 < \theta_{k1} < 1$ and $0 < \theta_{k2} < 1$.

Again, the boundary values of the estimate of states and perturbations are limited by $|\hat{P}_k| \leq |P_k^*|$, $|\hat{\Psi}_{k1}(\cdot)| \leq |P_k^*|/\Delta$, $|\hat{Q}_k| \leq |Q_k^*|$, and $|\hat{\Psi}_{k2}(\cdot)| \leq |Q_k^*|/\Delta$, respectively. The overall control structure of PORPC (15) and (24) is illustrated by Fig. 2, in which only the measurement of active power P_k and reactive power Q_k at the inverter side, as well as the DC voltage $V_{\mathrm{dc}1}$ and reactive power Q_1 at the rectifier side is needed for the controller and observer design. Note that their references are given by the power system operators to satisfy the practical transmission of electrical power or maintain power system stability through VSC-MTDC systems. Lastly, the obtained control inputs are modulated by the pulse width modulation (PWM) technique [21].

4 Case Studies

PORPC is applied on a three-terminal radial VSC-MTDC system demonstrated by Fig. 1, the corresponding controller parameters are tuned to improve the robustness in the presence of time-varying wind farm power outputs and weak

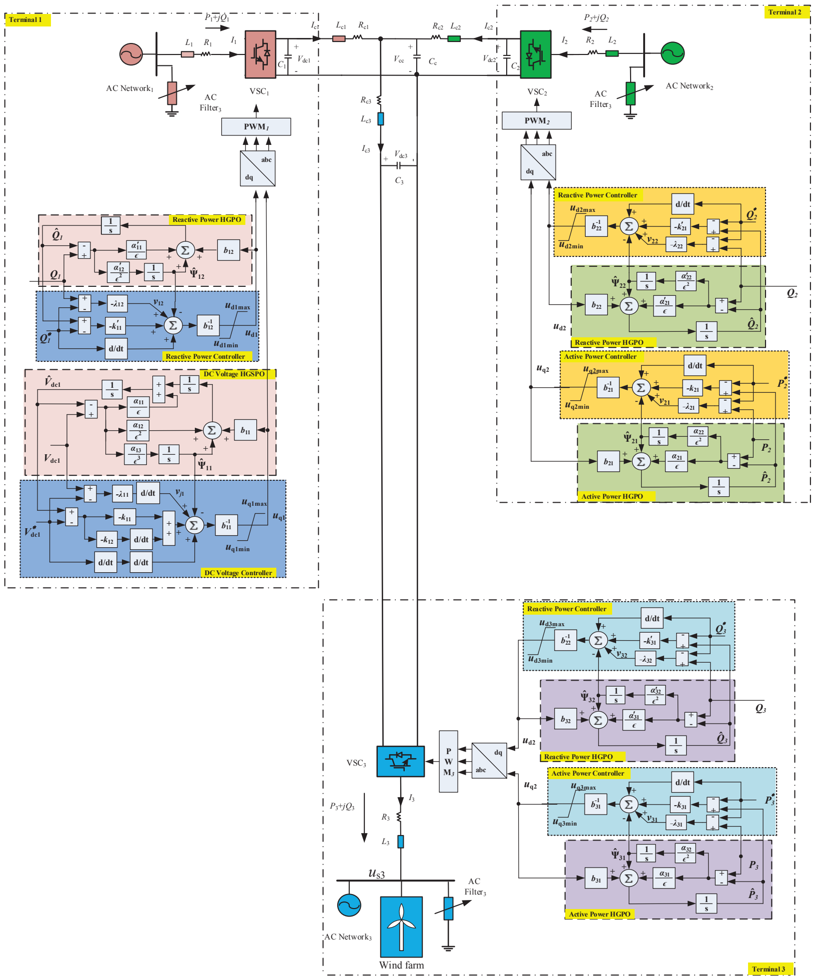

Figure 2: Overall control structure of PORPC for the VSC-MTDC systems.

grids connection. The three-terminal radial VSC-MTDC system parameters and the control parameters of PORPC are given in Table 1 and Table 2, respectively. The control performance of PORPC is evaluated under various operating conditions in a wide neighborhood of initial operating points, and compared to that of PI control [5, 22]and PC [12]. Due to the security requirement of converters, the control inputs are bounded as $|u_{\mathrm{q}1}| \leq 0.8$ per unit (p.u.), $|u_{\mathrm{d}1}| \leq 0.6$ p.u., $|u_{\mathrm{q}k}| \leq 0.8$ p.u., and $|u_{\mathrm{d}k}| \leq 0.6$ p.u., respectively [23].

Remark 2. For the observer gains shown in Table 1, they usually range from $10^3 - 10^5$ to provide a proper trade-off between estimation speed and peak value [14]. A larger observer gain will accelerate the estimation rate but also produce a higher peak value at the moment when system operation condition

Table 1: System parameters used in the simulation

AC grids frequency	f	50 Hz
AC grids base voltage	$V_{\mathrm{AC}_{\mathrm{base}}}$	100 kV
DC base voltage	$V_{\mathrm{DC}_{\mathrm{base}}}$	200 kV
System base power	S_{base}	100 MVA
AC grids resistance (25 km)	R_1, R_2, R_3	0.05 Ω/km
AC grids inductance (25 km)	L_1, L_2, L_3	0.026 mH/km
DC cable resistance (50 km)	R_0	0.21 Ω/km
DC bus capacitance	C_1, C_2, C_3	11.94 μF
Common DC capacitance	C_{c}	19.95 μF

Table 2: Control parameters used in the three-terminal VSC-MTDC system.

Rectifier controller parameters			
$k_{11} = 120$	$k_{12} = 25$	$\lambda_{11} = 5$	$b_{11} = 2$
$b_{12} = 0.05$	$k'_{11} = 75$	$\lambda_{12} = 5$	
Rectifier observer parameters			
$\alpha_{11} = 1250$	$\alpha_{12} = 5.2 \times 10^5$	$\alpha_{13} = 6.7 \times 10^7$	$\alpha'_{11} = 420$
$\alpha'_{12} = 5 \times 10^4$	$\Delta = 0.05\ s$	$\epsilon = 0.1$	
Inverter controller parameters, $k = 2, 3$			
$k_{k1} = 75$	$k'_{k1} = 75$	$b_{k1} = 0.1$	$b_{k2} = 0.1$
$\lambda_{k1} = 6$	$\lambda_{k2} = 6$	$\rho_k = 0.04$	
Inverter observer parameters, $k = 2, 3$			
$\alpha_{k1} = 410$	$\alpha_{k2} = 5 \times 10^4$	$\alpha'_{k1} = 420$	$\alpha'_{k2} = 4 \times 10^4$
$\Delta = 0.05\ s$	$\epsilon = 0.1$		

varies, while a smaller observer gain would not effectively track the output thus degrade the estimation performance significantly. This paper chooses them to be 1250 through trial-and-error among this range. For the control gains, they are chosen as so to provide a proper trade-off between the control costs and tracking speed. A too large control gain will rapidly track the output but also result in higher control costs, while a too small control gain might not control the output fast enough but with low control costs. This paper select them to be 75 for active power though trial-and-error, respectively. Note that a fast active power is preferred here as it is important to respond quickly for the purpose of power support.

4.1 Power regulation

The initial active power of the converter station 2 and 3 are both 40 MW. At 0.5 s, the active power reference of converter station 2 is decreased to 30 MW. And after 0.3 s, the active power reference of converter station 2 is further decreased to 20 MW. Meanwhile, the active power reference of converter 3 is increased to 50 MW at 1.7 s. After 0.3 s, the active power reference of converter 2 is further increased to 60 MW. While DC voltage of the rectifier V^*_{dc1} is regulated at the rated value. The system responses are provided by Fig. 3. When $t = 0.5$ s, the active power of the converter station 2 decreases from 40 MW to 30 MW.

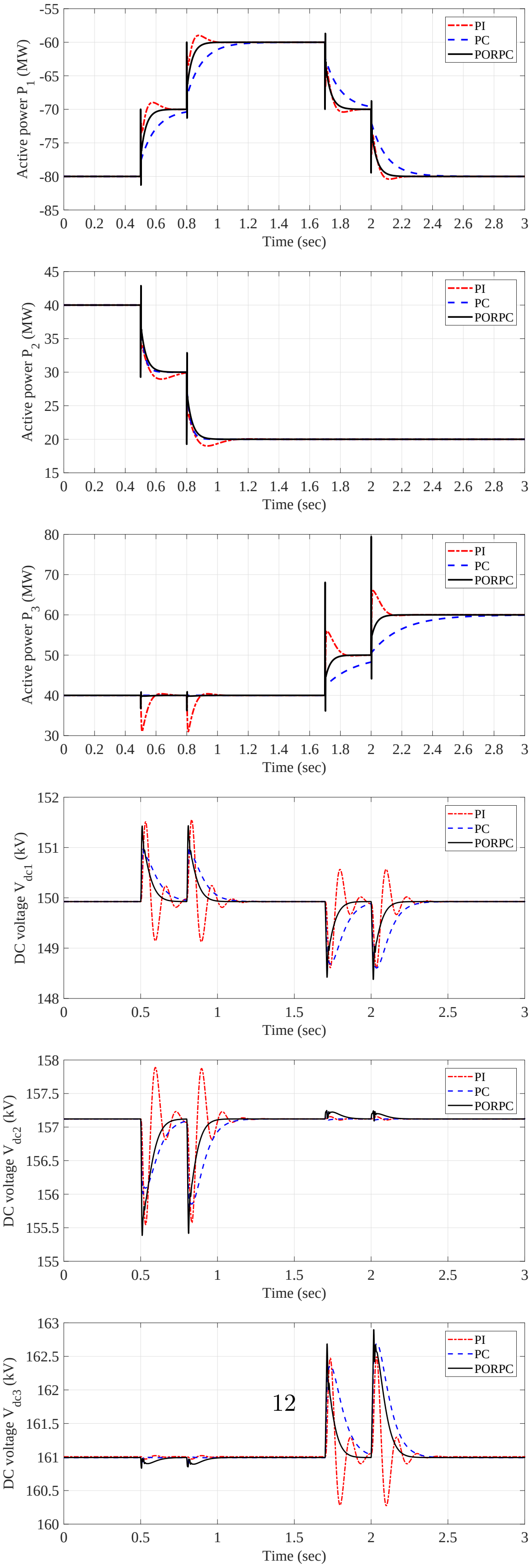

Figure 3: System responses obtained under normal operation condition.

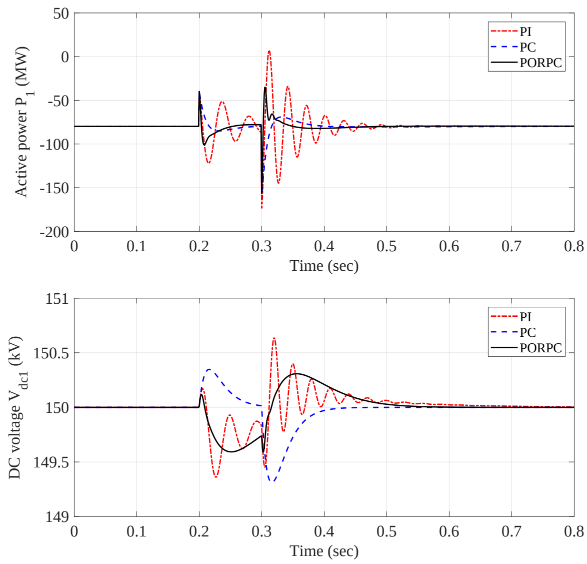

Figure 4: System responses obtained under the 10-cycle LLLG fault at AC bus 1.

Thus, the active power of the converter station 1 increases to -70 MW resulted from power balance. The converter stations 1 realizes the power balance and the DC voltage control. The active power is -80 MW initially. When $t = 0.8$ s, the active power of the converter station 2 decreases from 30 MW to 20 MW. Thus, the active power of the converter station 1 increases to -60 MW. When $t = 1.7$ s, the active power of the converter station 3 increased from 40 MW to 50 MW. Thus, the active power of the converter station 1 decreases to -70 MW. When $t = 2.0$ s, the active power of the converter station 3 decreased from 50 MW to 60 MW. Thus, the active power of the converter station 1 decreases to -80 MW.

From the above analysis, one can find that the overshoot of active and reactive power is completely eliminated by PC and PORPC compared to that of PI control, which is resulted from the full compensation of nonlinearities. Note that PORPC can achieve as satisfactory control performance as that of PC due to the real-time perturbation compensation, their tiny difference is caused by the estimation error when the power tracking starts.

4.2 10-cycle line-line-line-ground (LLLG) fault at AC buses

A 10-cycle LLLG fault occurs at AC bus 1 from 0.2 s to 0.3 s. Due to the fault, the voltage at AC bus 1 is decreased to a critical level. Fig. 4 shows that PORPC and PC can rapidly restore the system with less active power

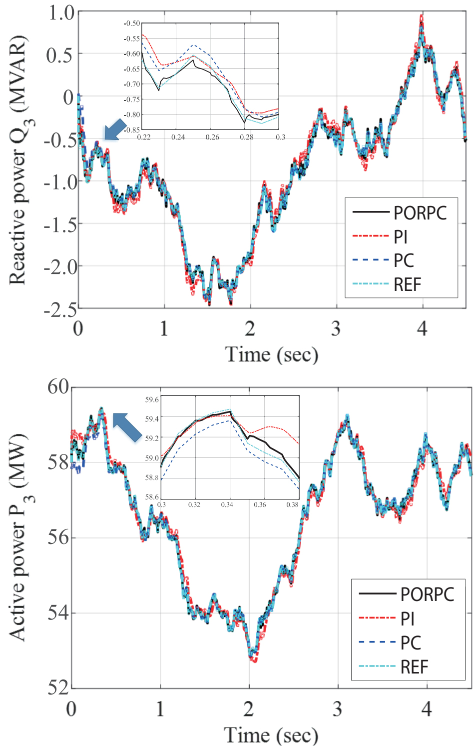

Figure 5: System responses obtained when an offshore wind farm is connected to the VSC-MTDC system.

oscillations than PI control. Thus, PORPC can effectively restore the disturbed VSC-MTDC system as an extra system damping is injected.

4.3 Offshore wind farm connection

In order to investigate the effect of the high percentage penetration of wind power [24, 25] into the VSC-MTDC system, AC network$_3$ is connected to an offshore wind farm. Under such framework, the power grid with offshore wind farm generate time-varying wind power variation which results in a fluctuated power flow at DC terminal. To study this circumstance, a wind speed oscillation occurs from 0 s to 4 s using auto-regressive and moving average (ARMA) time series models [26] is simulated. As illustrated in Fig. 5, it shows that PORPC can effectively track the active and reactive power. As PORPC does not need an accurate VSC-MTDC system model, an improved control performance can be achieved compared to that of other two methods.

4.4 Weak power grid connection

Weak power grids are generally defined by the following two aspects [27,28]: (1) Low effective short circuit ratio (ESCR) which means the impedance relative to the DC power is high, and (2) Low effective DC inertia constant H_{dc} which means the inertia of AC system is low. The ESCR is defined as $\frac{S-Q_{\mathrm{c}}}{P_{\mathrm{d}}}$ where S is the AC system three-phase symmetrical short-circuit level in MVA at the HVDC converter terminal at AC side. Here, P_{d} is the rated DC terminal power in MW, and Q_{c} is the value of three phase fundamental Mvar of all shunt filters and capacitor banks on the bus bar that are connected. The effective inertia constant H_{dc} is defined as $H\frac{S}{P_{\mathrm{d}}}$ where H is conventional inertia constant of the machine in the AC grid [29]. The power grids with ESCR less than 2.5 are defined as high impedance systems. The AC system with H_{dc} less 2 are defined as inadequate inertia system which has limited generation and cannot maintain the normal frequency deviation (less than 5%) [29]. This case attempts to investigate the system performance when the system is made progressively weaker by decreasing effective DC inertia constant and ESCR of the AC grid with reduction of H and increase of impedance of the grid, respectively. A strong power grid which ESCR equals 4.3 and H_{dc} equals 2.7, while a weak power grid which ESCR equals 2.1 and H_{dc} equals 1.7 are connected to terminal 2 during simulation, respectively. The control performance of the test results are provided in Table 3.

4.5 Comparative studies

To compare the control performance of each schemes in all four cases, the integral of absolute error (IAE) index is calculated and provided in Table 3. Here $\mathrm{IAE}_{Q_1} = \int_0^T |Q_1 - Q_1^*|\mathrm{d}t$, $\mathrm{IAE}_{V_{\mathrm{dc1}}} = \int_0^T |V_{\mathrm{dc1}} - V_{\mathrm{dc1}}^*|\mathrm{d}t$, $\mathrm{IAE}_{Q_2} = \int_0^T |Q_2 - Q_2^*|\mathrm{d}t$, $\mathrm{IAE}_{P_2} = \int_0^T |P_2 - P_2^*|\mathrm{d}t$, $\mathrm{IAE}_{Q_3} = \int_0^T |Q_3 - Q_3^*|\mathrm{d}t$ and $\mathrm{IAE}_{P_3} = \int_0^T |P_3 - P_3^*|\mathrm{d}t$. The units of system variables are p.u.. The simulation time $T = 6$ s such that all system states can converge to the equilibrium point. Note that PORPC has a little bit higher IAE than PC under the nominal model due to the estimation error, while PORPC has similar IAE compared to PI control in the presence of system parameter uncertainties. However, IAE_{Q_1}, $\mathrm{IAE}_{V_{\mathrm{dc1}}}$, IAE_{Q_2}, IAE_{P_2}, IAE_{Q_3} and $\mathrm{IAE}_{P_3}$of PORPC are only 15.93%, 4.68%, 13.69%, 12.87%, 13.92% and 13.3% of that of PC. Furthermore, PORPC provides greater system damping as it has the lowest IAE when the 10-cycle LLLG fault at AC buses occurs. In particular, IAE_{Q_1} and $\mathrm{IAE}_{V_{\mathrm{dc1}}}$ of NAC are only 21.14% and 21.2% of those of PI control when the fault occurs at AC bus 1, while IAE_{Q_2} and IAE_{P_2} of PORPC are only 19.49% and 27.92% of those of PI control when the fault occurs at AC bus 2. Finally, the overall control efforts of different approaches are also presented, here $\mathrm{IAE}_u = \int_0^T \sum_{i=0}^{n=3}(|u_{\mathrm{q}i}| + |u_{\mathrm{d}i}|)dt$, one can find PORPC needs similar control efforts to that of PI control and PC but provides great robustness.

Table 3: IAE index of different control schemes

IAE index in VSC-HVDC			
Case / Method	Power Regulation		
	PI	PC	PORPC
IAE_{Q_1}	4.18E-02	3.26E-02	3.49E-02
$IAE_{V_{dc1}}$	6.54E-03	5.16E-03	5.28E-03
IAE_{Q_2}	3.05E-02	2.41E-02	3.02E-02
IAE_{P_2}	3.80E-02	2.83E-02	3.03E-02
IAE_{Q_3}	3.07E-02	2.43E-02	2.99E-02
IAE_{P_3}	3.82E-02	2.89E-02	3.04E-02
IAE_u	2.68E-01	2.88E-01	3.10E-01
Case / Method	10-cycle LLLG Fault		
	PI	PC	PORPC
IAE_{Q_1}	2.62E-01	1.13E-01	5.54E-02
$IAE_{V_{dc1}}$	1.75E-01	1.02E-01	3.71E-02
IAE_{Q_2}	3.53E-01	2.48E-01	6.88E-02
IAE_{P_2}	2.93E-01	3.07E-01	8.18E-02
IAE_{Q_3}	3.52E-01	2.47E-01	6.89E-02
IAE_{P_3}	2.92E-01	3.05E-01	8.19E-02
IAE_u	1.48E-01	1.11E-01	1.14E-01
Case / Method	Offshore Wind Farm Connection		
	PI	PC	PORPC
IAE_{Q_3}	6.63E-02	6.84E-02	2.16E-02
IAE_{P_3}	7.67E-02	1.04E-01	1.27E-02
IAE_u	3.32E-02	2.99E-02	3.15E-02
Case / Method	Strong Power Grid Connection		
	PI	PC	PORPC
IAE_{Q_2}	5.13E-02	4.86E-02	2.62E-02
IAE_{P_2}	5.71E-02	2.85E-01	2.17E-02
IAE_u	2.92E-02	2.89E-02	2.35E-02
Case / Method	Weak Power Grid Connection		
	PI	PC	PORPC
IAE_{Q_2}	7.15E-02	6.46E-02	7.23E-02
IAE_{P_2}	8.91E-02	3.24E-01	4.73E-02
IAE_u	4.02E-02	4.19E-02	3.67E-02

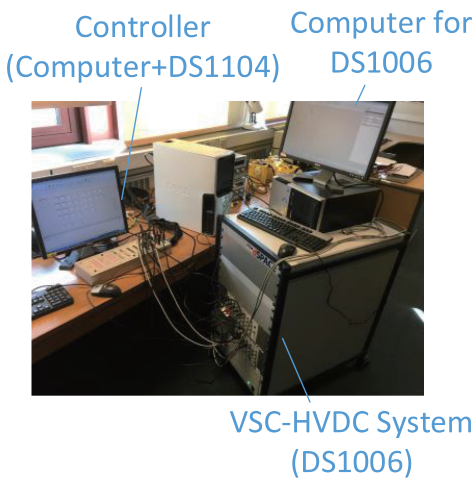

Figure 6: The experiment platform of the HIL test.

5 Hardware-in-the-loop Test

A dSPACE simulator based HIL real-time implementation test is carried out to test the implementation feasibility of PORPC, while the experiment platform is demonstrated in Fig. 6. The whole system is modelled with multiple sampling rates. The time resolution of the gating signals of industrial controllers is normally a few microseconds [30] which is far bigger than real-time simulation sampling steps. The rectifier controller (15) and inverter controller (24) are implemented on one DSP board (dSPACEDS1104) with a sampling frequency $f_c = 0.5$ kHz, and the VSC-MTDC system is simulated on another dSPACE platform (DS1006 board) with the limit sampling frequency $f_s = 50$ kHz to make HIL simulator as close to the real plant as possible. The measurements of the reactive power Q_1, DC voltage V_{dc1}, active power P_2, reactive power Q_2, active power P_3 and reactive power Q_3 are obtained from the real-time simulation of the VSC-MTDC system on the DS1006 board, which are sent to three controllers implemented on another DSP (dSPACEDS1104) board for the control outputs calculation.

5.1 HIL test: power regulation

The references of active power of converter 2 changes at $t = 0.3$ s, $t = 0.6$ s and finally decreases to 20 MW. Meanwhile, the reference of active power of converter 3 changes at $t = 1.9$ s, $t = 2.2$ s and finally increases to 60 MW, while DC voltage is regulated at the rated value $V_{dc1}^* = 150$ kV as similar as case studies investigated in section 4. The system responses of HIL test and simulation are compared by Fig. 7, which shows HIL test results have almost the same performance as that of the simulation results. Note that when the

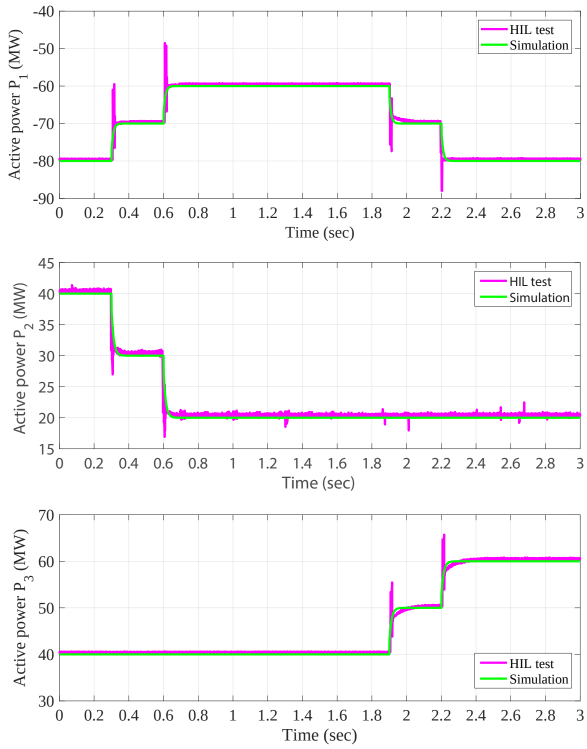

Figure 7: HIL test results of system responses obtained under the normal operation condition.

active power of the converter station 2 changes such as at 0.3s, the active power of the converter station 2 decreases from 40 MW to 30 MW, the active power of the converter station 1 increases to -70 MW rapidly with some unavoidable propagated overshoot to keep the power balance.

5.2 HIL test: 10-cycle line-line-line-ground (LLLG) fault at AC bus 1.

A 10-cycle LLLG fault occurs at AC bus 1 when $t = 0.1$ s. Fig. 8 demonstrates that the disturbed system can be rapidly restored as expected in section 4. The system responses obtained by the HIL test is similar to that of simulation results with some communication glitches. Note that there is only tiny difference between simulation result and HIL test result in V_{dc1} caused by the measurement noise (less than 0.34%).

Remark 1. The difference between the simulation and HIL test demonstrated in Fig. 7 and Fig. 8 is mainly resulted from the following three reasons: (i) Some measurement disturbances exist in HIL test which are not regarded

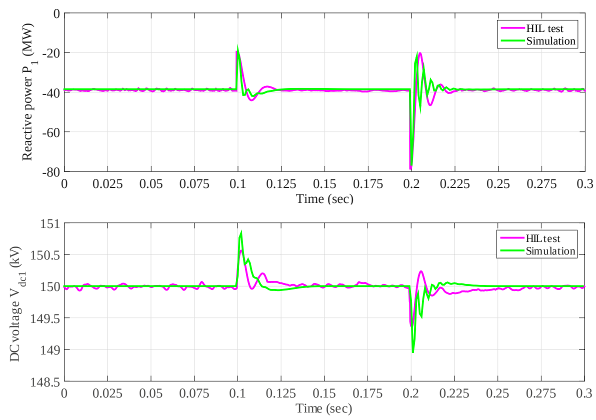

Figure 8: HIL test results of system responses obtained under the 10-cycle LLLG fault at AC bus 1.

in the simulation, a filter can be applied to remove it and improve the control performance; (ii) The sampling holding and discretization of HIL test might introduce additional errors compared to the continuous control in the simulation; and (iii) The existence of time delay of the real-time controller, whose exact value is unlikely to obtain. A time delay $\tau = 2$ ms is assumed in the simulation.

6 Conclusions

This paper develops a PORPC for the VSC-MTDC system with integrated offshore wind farm to improve the robustness against power fluctuation, system disturbances. The main conclusions can be summarized as the following three points:

(a) The combinatorial effect of system nonlinearities, parameter uncertainties, unmodelled dynamics and external disturbances, e.g., grid faults and time-varying wind power output, is aggregated into a perturbation, which is fully estimated by PO and compensated by PORPC, such that a considerable robustness and improved system damping with reasonably low control efforts can be simultaneously achieved via passification;

(b) PORPC does not require an accurate VSC-MTDC system model and only the reactive power and active power at inverter side, while DC voltage and reactive power at rectifier side need to be measured. Besides, a DC link voltage droop controller is employed to greatly improve the immediate response to the grid unbalanced conditions. Future study will be focused on employing optimization algorithms, e.g., genetic algorithm (GA) or particle swarm optimization (PSO), to optimize the parameters selection procedure of PORPC;

(c) Four case studies have been undertaken to evaluate the control performance of the proposed approach, including power regulation, AC bus fault, offshore wind farm integration, and weak power grids connection, respectively. Simulation results verify that PORPC can maintain consistent control performance and provide significant robustness under various operation conditions of VSC-MTDC with wind farm integration. Moreover, an HIL test has been carried out through dSPACE simulator which validates the implementation feasibility of the proposed scheme.

Acknowledgements

The authors gratefully acknowledge the support of Yunnan Provincial Talents Training Program (KKSY201604044) and Scientific Research Foundation of Yunnan Provincial Department of Education (KKJB201704007).

References

[1] Xu, L. and Yao, L.: 'DC voltage control and power dispatch of a multi-terminal HVDC system for integrating large offshore wind farms', *IET Renew. Power Gener.*, 2011, **5**, (3), pp. 223-233

[2] Bresesti P., Kling W. L., Hendriks R. L., and Vailati R.: 'HVDC connection of offshore wind farms to the transmission system', *IEEE Trans. Energy Convers.*, 2007, **22**, pp. 37-43.

[3] Flourentzou N., Agelidis V. G., and Demetriades G. D.: 'VSC-based HVDC power transmission systems: an overview', *IEEE Trans. Power Electron.*, 2009, **24**, pp. 592-602.

[4] Li X., Yuan Z., Fu J., Wang Y., Liu T., and Zhu Z.: 'Nanao multiterminal VSC-HVDC project for integrating large-scale wind generation', *Proc. IEEE Power Energy Soc. Gen. Meeting Conf. Expo.*, Jul. 2014.

[5] Li S., Haskew T. A., and Xu L.: 'Control of HVDC light system using conventional and direct current vector control approaches,' *IEEE Trans. Power Electron.*, 2010, pp. 3106-3118.

[6] Ruan S. Y., Li G. J., Jiao X. H., Sun Y. Z., and Lie T.: 'Adaptive control design for VSC-HVDC systems based on backstepping method,' *Elect. Power Syst. Res.*, 2007, **77**, pp. 559-565.

[7] Moharana A. and Dash P. K.: 'Input-output linearization and robust sliding-mode controller for the VSC-HVDC transmission link,' *IEEE Trans. Power Del.*, 2010, **25**, (3), pp. 1952-1961.

[8] Chaudhuri N. and Chaudhuri B.: 'Adaptive droop control for effective power sharing in multi-terminal DC (MTDC) grids', *IEEE Trans. Power Syst.*, 2013, **28**, (1), pp. 21-29.

[9] Zhao X. and Li K.: 'Adaptive backstepping droop controller design for multi-terminal high-voltage direct current systems', *IET Gener. Transm. Distrib.*, 2015, **9**, (10), pp. 975-983.

[10] Stamatiou G. and Bongiorno M.: 'Power-dependent droop-based control strategy for multi-terminal HVDC transmission grids', *IET Gener. Transm. Distrib.*, 2017, **11**, (2), pp. 383-391.

[11] Yang B., Jiang L., Yao W., and Wu Q.H.: 'Perturbation estimation based adaptive coordinated passive control for multimachine power systems', *Control Eng. Pract.*, 2015, **44**, pp. 172-192.

[12] Harnefors L., Yepes A., Vidal A., and Doval J.: 'Passivity-based controller design of grid-connected VSCs for prevention of electrical resonance instability', *IEEE Trans. Ind. Electron.*, 2015, **62**, (2), pp. 702-710.

[13] Chen J., Jiang L., Yao W., and Wu Q.: 'Perturbation estimation based nonlinear adaptive control of a full-rated converter wind turbine for fault ride-through capability enhancement', *IEEE Trans. Power Syst.*, 2014, **29**, (6), pp. 2733-2743.

[14] Yang, B., Jiang, L, Yao, W., and Wu, Q.H.: 'Perturbation observer based adaptive passive control for damping improvement of multi-terminal voltage source converter-based high voltage direct current systems', *Transactions of the Institute of Measurement and Control*, 2017, **39**, (9), pp. 1409-1420.

[15] Torres-Olguin, R.E., Molinas, M., Undeland, T.: 'Offshore wind farm grid integration by VSC technology with LCC-based HVDC transmission', *IEEE Trans. Sustain. Energy*, 2012, **3**, (4), pp. 899-907.

[16] Heier S. and Waddington R.: *Grid Integration of Wind Energy Conversion Systems*, New York: Wiley, 2006.

[17] Slootweg, J.G., de Haan, S.W.H., Polinder, H., Kling, W.L.: 'General model for representing variable speed wind turbines in power system dynamics simulations'. *IEEE Trans. on Power Syst.*, 2003, **18**, (1), pp. 144-151.

[18] Yang B., Yu T., Shu H. C., Dong J., and Jiang L.: 'Robust sliding-mode control of wind energy conversion systems for optimal power extraction via nonlinear perturbation observers', *Applied Energy.* http://dx.doi.org/10.1016/j.apenergy.2017.08.02

[19] Yang B., Jiang L., Wang L., Yao W., Wu Q.H.: 'Nonlinear maximum power point tracking control and modal analysis of DFIG based wind turbine', *International Journal of Electrical Power and Energy Systems*, 2016, **74**, pp. 429-436.

[20] Haileselassie, T.M., Uhlen, K.: 'Impact of DC line voltage drops on power flow of MTDC using droop control', *IEEE Trans. Power Syst.*, 2012, **27**, (3), pp. 1441-1449

[21] Wu F. J., Sun, D. Y., and Duan, J. D.: 'Diagnosis of single-phase open-line fault in three-phase PWM rectifier with LCL filter', *IET Gener. Transm. Distrib.*, 2016, **10**, (6), pp. 1410-1421.

[22] Yazdani A., Iravani R.: 'Dynamic model and control of the NPC-based back-to-back HVDC system', *IEEE Trans. Power Del.*, 2006, **21**, (1), pp. 414-424

[23] Jovcic D. and Ahmed K.: 'High-voltage direct-current transmission: converters, systems and DC grids', *Wiley-Blackwell*, first edition. Jul. 2015.

[24] Liu J., Wen J. Y., Yao W., Long Y.: 'Solution to short-term frequency response of wind farms by using energy storage systems', *IET Renewable Power Generation*, 2016, **10**, (5), pp. 669-678.

[25] Liao S. W., Yao W., Han X. N., Wen J. Y., Cheng S. J.: 'Chronological operation simulation framework for regional power system under high penetration of renewable energy using meteorological data', *Applied Energy*, 2017, **203**, pp. 816-828.

[26] Wang, P., Billinton, R.: 'Reliability benefit analysis of adding WTG in a distribution system', *IEEE Trans. Energy Convers.*, 2001, **16**, (2), pp. 134-139.

[27] Kundur P. *Power System Stability and Control*, New York: McGrawHill, 1994.

[28] Babazadeh, D., Muthukrishnan, A., Mitra, P., Larsson, T., Nordstrm, L., 'Real-time estimation of AC-grid short circuit capacity for HVDC control application', *IET Gener. Transm. Distrib.* 2017, **11**, (4), p. 838-846,

[29] Yogarathinam B., Kaur J., and Chaudhuri N., 'Impact of inertia and effective short circuit ratio on the control of frequency in weak grids interfacing LCC-HVDC and DFIG-based wind farms', *IEEE Trans. Power Del.*, 2017, **32**, (4), pp. 2040-2051.

[30] Li W.and Belanger J.,'An FPGA-based Real-time HIL Test Bench for Full-Bridge Modular Multilevel STATCOM Controller',*2015 17th European Conference on Power Electronics and Applications (EPE'15 ECCE-Europe)* Sep. 2015.